Numerical and Experimental Investigations of a Generic Rocket Launcher Configuration with Cold Plume in Hypersonic Flow

Kai Oßwald, Volker Hannemann* and Klaus Hannemann**
*Sören Stephan** and Rolf Radespiel***
**Institute of Aerodynamics and Flow Technology, DLR*
Bunsenstraße 10, 37073 Göttingen, Germany
***Institute of Fluid Mechanics, Technische Universität Braunschweig*
38108 Braunschweig, Germany

Abstract
A generic rocket launcher geometry is studied experimentally and numerically at hypersonic flow conditions including a cold plume. The experiments are conducted in a hypersonic Ludwieg tube while numerical calculations are performed with a finite-volume Navier-Stokes solver using the Detached-Eddy Simulation technique. Good agreement for the mean flow field is obtained. However, discrepancies between the spectral analysis of the computed and measured pressure fluctuations are observed.

1 Introduction

Base buffeting can be a major problem for space launchers during atmospheric ascent [1]. Massively separated flow in the launcher's base region causes strong dynamic loads on the vehicle's nozzle. Progress in the understanding of the flow phenomena benefits from a close cooperation of experimental and numerical studies in order to improve the measurement techniques as well as the numerical methods with respect to base buffeting simulations. A collaboration of numerical and experimental working groups is established within the framework of the DFG-Sonderforschungsbereich Transregio 40 "*Technological foundations for the design of thermally and mechanically highly loaded components of future space transportation systems*". The research within the Transregio 40 is partly dedicated to base flow investigations. A subsonic ($Ma = 0.2$) and a supersonic ($Ma = 6$) setup are considered in the first project period. The flow past the generic rocket launcher configuration is investigated with and without underexpanded plume emanating from the nozzle.

On the experimental side, the optical access to the flow field is used for instantaneous pictures such as Schlieren and field measurement techniques such as Particle Image Velocimetry (PIV). A Pitot rake survey of the mean flow is performed. The unsteady behaviour of the flow is captured in shape of high resolution wall pressure signals. On the numerical side, simulations of steady state Reynolds-averaged Navier-Stokes (RANS) solutions [2] to time-resolved Detached-Eddy Simulations (DES) and zonal Large-Eddy Simulations (LES) are conducted.

Two numerical and three experimental groups were involved in the first project phase. The unsteady behavior of the supersonic configuration was primarily investigated by DLR Cologne in a long duration hypersonic wind tunnel and numerically simulated with the zonal LES approach of RWTH Aachen [3]. The subsonic experiments conducted at RWTH Aachen were the focus of the numerical DLR group involved in the present work [4]. The experimental group of the Technische Universität Braunschweig studied in close cooperation with the University of the Bundeswehr in Munich the feasibility of PIV measurements in a short duration hypersonic facility [5].

As a common configuration for the two hypersonic facilities and both numerical methods, a generic rocket launcher configuration was chosen including a cold plume in a hypersonic ambient flow. In order to complete the previous investigation [3] experiments were conducted in the Hypersonic Ludwieg Tube Braunschweig (HLB) and the respective DES calculated utilizing the DLR-TAU code. The focus of the present study was put on (i) time-accurate measurements in a short duration wind tunnel, (ii) different numerical schemes and

setup (DES instead of zonal LES) and (iii) grid resolution study with respect to the plume shear layer. The preliminary results of the on-going work are shown and discussed.

2 Experimental Setup

The generic rocket launcher configuration presented in Fig. 1 is considered in both the experimental and numerical investigations. The length ratios of the afterbody of this geometry are derived from the European launcher Ariane 5 to reproduce a similar base flow including the driving flow features. The main body of the generic rocket model geometry consists of a blunted cone with a nose radius of 10 mm and a cone angle of 36° followed by a 328.6 mm long cylinder with diameter $D = 108\,mm$. A TIC-nozzle (truncated ideally contour) is attached in the center of the main body's base area. The outer shape of the centered nozzle is a cylinder which has a diameter of $0.4D$ and a length of $1.2D$. A support on the main body keeps the model at a fixed position inside the wind tunnel and supplies test gases needed for the plume generation via internal pipes. The support geometry consists of two parallel surfaces with a leading and trailing wedge and is mounted orthogonally to the main body.

Figure 1: Sketch of generic rocket model with transparent nozzle to visualize the inner contour.

The ambient flowfield has a freestream Mach number of 6 and a unit Reynolds number of $16 \times 10^6\,m^{-1}$. In combination with boundary layer tripping, a fully turbulent boundary layer is expected to develop on the main body before separating at the shoulder of the base. In the present investigations a cold plume is considered which means that the stagnation temperature of the nozzle flow is similar to the stagnation temperature of the freestream. To reach an area-averaged Mach number of 2.5 across the exit plane a stagnation pressure of 20 bar is needed.

Table 1: Nominal flow conditions.

	$P_0\,[Pa]$	$T_0\,[K]$	Ma_∞	Re $[1/m]$
Freestream	16.8×10^5	470	6.0	16×10^6
Nozzle flow	20×10^5	470	-	-

2.1 HLB

Figure 2 shows a schematic of the Hypersonic Ludwieg Tube Braunschweig (HLB). The HLB is a cold Ludwieg tube blow down tunnel with a fast acting valve. This valve separates the high pressure and the low pressure parts of the facility. The high pressure part consists of the 17 m long storage tube with a 3 m heated part. The maximum pressure in the storage tube is 30 bar. The low pressure part consists of the $Ma = 5.9$ Laval nozzle, the 0.5 m circular test section, the diffuser and the dump tank. Prior to running the facility the low pressure section is evacuated to a few $mbar$. The measuring time is up to 80 ms during which almost constant flow conditions are obtained. The unit Reynolds number range of the facility is (3 to 20)$\times 10^6\,1/m$. More detailed information on the construction and operation of the HLB are given by Estorf [12].

For jet simulation the jet simulation facility is attached onto the HLB. A sketch of the jet simulation facility is shown in Fig. 3(a). The working principle is similar to the HLB wind tunnel as this is a Ludwieg tube blow down tunnel with a fast acting valve as well. Outside of the HLB test section is the 32 m long heated storage tube. The diameter of the storage tube is 18.88 mm and it can be pressurized up to 140 bar and heated up to 900 K. In the jet simulation facility nozzle exit the flow reaches a Mach number of 2.5. More detailed information on the design and operation of the jet simulation facility are given by Stephan [13].

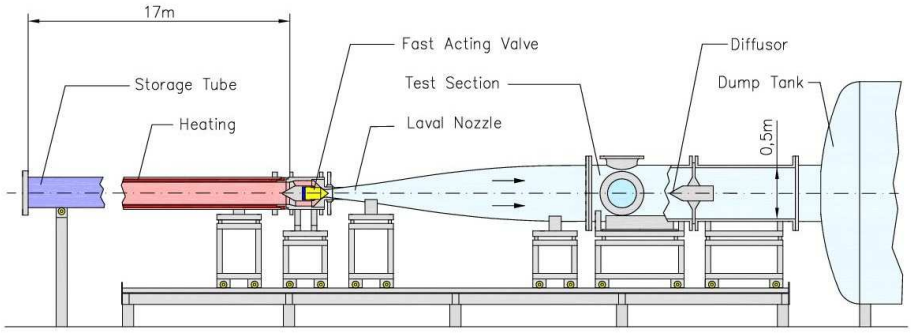

Figure 2: Schematic of the Hypersonic Ludwieg Tube Braunschweig (HLB).

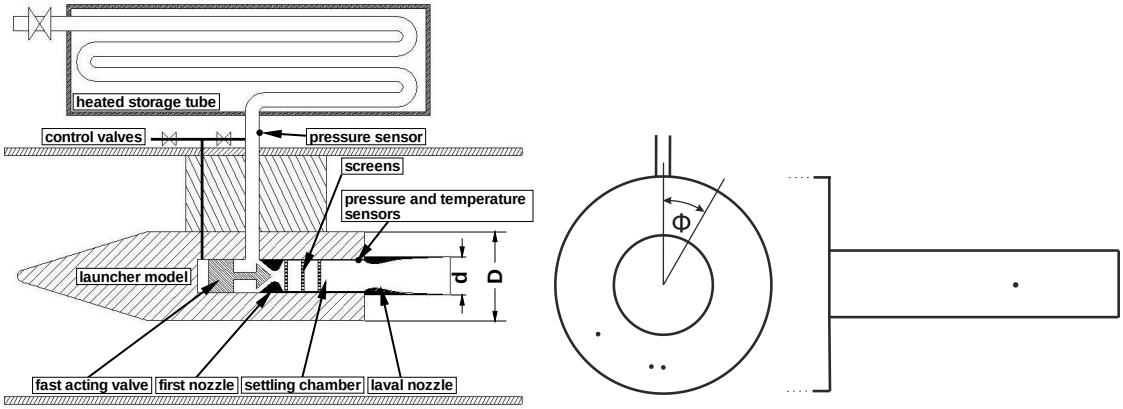

(a) Sketch of the jet simulation facility. The diameters are $d = 43\,mm$ (nozzle) and $D = 108\,mm$ (cylindrical model).

(b) Pressure sensor positions indicated by points on the base and on the nozzle dummy.

Figure 3: Sketches of the jet simulation facility and the sensor positions in the HLB experiment.

The jet simulation facility is instrumented with pressure and temperature sensors. The locations of the storage tube pressure sensor and the sensors in the settling chamber are shown in Fig. 3(a). A Gefran (Type: TKDA-N-1-Z-B16D-M-V) transducer is used for measuring the storage tube static pressure. The pressure range is between $0\,bar$ and $160\,bar$ and the response time for this transducer is less than $1\,ms$. For measuring the static pressure in the settling chamber three Kulites (XCEL-152) are used. The pressure range of these transducers is between $0\,bar$ and $34.5\,bar$, having a response time of less than $1\,ms$. The transducers are placed at the circumference with a 120 degree distance beginning from the top. In the settling chamber three temperature sensors are additionally placed at the circumference with a 120 degree distance beginning from the bottom. K-Type thermocouples (TJC100-CASS-IM025E-65 Sensor from Omega) are presently used for measuring the settling chamber temperature. The response time of the thermocouple with $0.04\,mm$ diameter wire is less than $20\,ms$.

The Pitot pressure at the nozzle exit and in the jet is measured with a rake consisting of 13 sensors. One sensor is located in the center of the nozzle exit. The other sensors are evenly distributed in two orthogonal sections. The distance between the sensors is $9mm$. Small and low cost transducers from Honeywell (True Stability Silicon Pressure Sensors Series Standard Accuracy) with a pressure range from $0\,bar$ to $10\,bar$ and $1\,ms$ response time are used in the Pitot rake.

For the unsteady base pressure measurement four Kulite sensors are flush mounted on the base and on the nozzle surface, see Figure 3(b). At the base three Kulite sensors (Type : XCS-093, pressure range $0.35\,bar$ absolute) are placed at the circumference at 180°, 190° and 240° beginning at the top. The distance from the centerline is $r = 45\,mm$. Another Kulite sensor is placed at the outer nozzle surface at 180° and $83\,mm$

downstream of the base. The pressure data was sampled with a Spectrum M2i.4652 transient recorder. The sampling frequency was set to 3 MHz and frequencies above 50 kHz were removed by applying a filter. For undisturbed flow a time trace of 40 ms is recorded and at least 10 tunnel runs are merged.

3 Numerical Method

The numerical flow field analysis for this study is performed via the Improved Delayed Detached-Eddy Simulation (IDDES) technique using the DLR TAU-code, a flow solver for the compressible Navier-Stokes equations [6]. The DLR TAU-code is a second-order finite-volume approach on hybrid structured and unstructured grids [7].

In this study the one-equation Spalart-Allmaras turbulence model is used as a baseline model for the DES. A three-stage explicit Runge-Kutta scheme is chosen as a relaxation solver within the multigrid iterations which are accelerated using local time stepping. The time accurate flow simulations are computed by a second-order Jameson type dual time stepping scheme. As an implicit algorithm it is not restricted in the choice of the smallest time step in the computational domain.

An AUSMDV upwind scheme is used with a MUSCL type reconstruction to achieve second order spatial accuracy. The numerical dissipation of the scheme at low Mach numbers is improved by changing the reconstructed velocities [9] following the ideas of Thornber et al. [8]. The left and right velocity vectors $\vec{u}_L$, $\vec{u}_R$ are modified in a subsonic situation linear to the Mach number in order to reach the arithmetic mean of the velocities at Mach number $Ma = 0$:

$$\begin{aligned} \vec{u}_L^* &= \frac{(1+z)\,\vec{u}_L + (1-z)\,\vec{u}_R}{2} \\ \vec{u}_R^* &= \frac{(1+z)\,\vec{u}_R + (1-z)\,\vec{u}_L}{2} \end{aligned} \quad \text{with } z = \min\left(1, \max(Ma_L, Ma_R)\right) \text{ and } Ma = \frac{|\vec{u}|}{a} \tag{1}$$

Here a denotes the speed of sound. Although only minor improvements have been observed with respect to the resolved vortical structures of the supersonic flow fields, the modification turns out to be beneficial for the convergence behavior within the dual time stepping.

To make use of the model's symmetry and thus reducing computational costs, the computational domain spans a 180° part of the geometry by applying a symmetry boundary condition in the vertical plane. The structured grid consists of about 11 million hexahedral cells. A cut through the symmetry plane of the computational domain is shown in Fig. 4(a) next to a close-up view of the grid in the base region (Fig. 4(b)).

To obtain a sufficient spatial resolution of the plume shear layer a cone region is refined near the nozzle exit, see Fig. 4(c). The cell size in the refined area is four times smaller than the original grid spacing. This leads to a grid with about 21 million cells which is almost a doubling in mesh size. One quarter of this adapted cone region as well as its foot print in the symmetry plane can be seen in the figure. The inner part of the adapted grid consists of hexahedra which are surrounded by tetrahedral and pyramidal cells to connect both structured parts of the grid without hanging nodes.

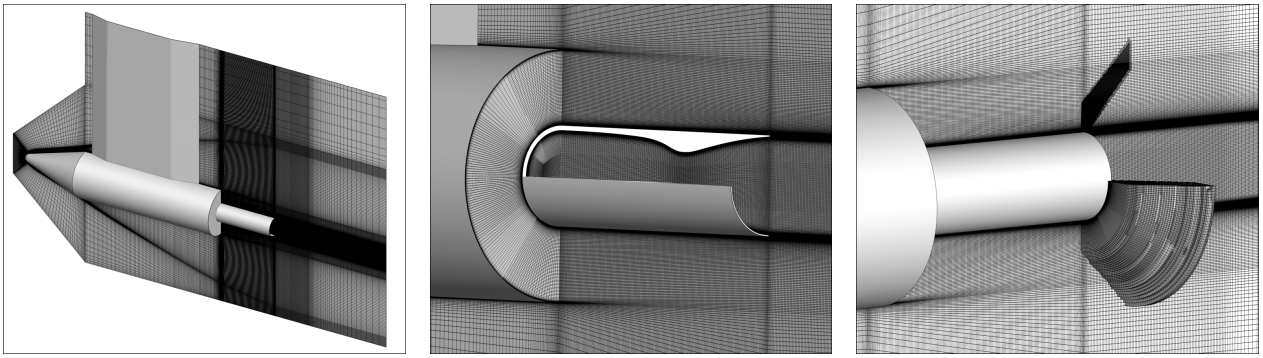

(a) Computational domain (b) Base region and nozzle interior grid (c) Adapted grid at nozzle exit

Figure 4: Computational grid used for the Detached-Eddy Simulation.

The applied Improved Delayed DES (IDDES) formulation combines the protection of the RANS mode operation in the boundary layer (referred to as DDES) with the ability to resolve the log-layer mismatch

existent in the original DES formulation when performing wall-modeled LES of attached flows. It was first proposed in [10]. For an extensive overview of DES formulations the reader is referred to [11].

The numerical simulation is set up with the nominal flow conditions specified in Table 1. A transition line is specified on the main body which nearly coincide with the foot print of the bow shock around the support. An experimental indication for this transition location was found in the other hypersonic facility in Cologne. It is assumed to fit for the same geometry at similar conditions in the HLB. No inflow profiles are used for the nozzle flow. Instead, the stagnation pressure and stagnation temperature taken from Table 1 are used as an inflow boundary condition for the nozzle chamber to establish the designed conditions at the nozzle exit.

A time step of $\Delta t = 5 \times 10^{-8}\, s$ is applied in the simulation, determined by the cell size in the base region and the freestream velocity. After a start-up phase the unsteady flowfield is well established and shows no longer artifacts from the steady state initial solution. From then on the averaging process of the mean values is started. Similar, the recording of the variances is turned on when the mean values are suitably converged. Overall, $3.3\, ms$ of time-accurate data including fluctuations is accumulated in the numerical simulation.

4 Results

The focus is on the base flow of the generic rocket model of Fig. 1. First, a short description of the overall flow topology is given by mean of Mach number distributions and Schlieren images. Then the influence of the model support and the Pitot pressure measurements in the plume region are discussed. A grid refinement study of the region near the nozzle exit is analyzed with respect to pressure fluctuations in the base flow. Finally, spectral analysis is performed of pressure signals recorded in the experiments and compared to numerical results.

4.1 Flow topology

In Fig. 5(a) the overall flow topology is illustrated by the mean Mach number distribution in the symmetry plane and isolines of the normalized pressure on the surface of the model. The bow shock in front of the blunted nose becomes conical along the front cone and is slightly curved when the expansion from the beginning of the cylindrical body reaches the shock. A weaker almost planar shock is generated by the support of the model. Both shocks interact in front of the support and the footprint of the conical shock is clearly visible in the pressure isolines on the support. The weak pressure trace on the cylindrical body originates from the interaction zone.

Vortical structures are generated by the support which are deflected downwards in circumferential direction as they travel along the main body, cf. Fig. 5(b). A second cluster of larger vortical structures is created by the interaction of the bow shock and the support which is of less interest since these vortical structures have no influence on the base region in contrast to those moving along the main body. The vortical structures are visualized using the Q-criterion

$$Q = \frac{1}{2}\frac{\partial u_i}{\partial u_j}\frac{\partial u_j}{\partial u_i} = \frac{1}{2}\left(\|\Omega\|^2 + \|S\|^2\right), \tag{2}$$

where the vorticity tensor Ω is the symmetric part of the velocity-gradient tensor ∇u and the strain-rate tensor S is the antisymmetric part. Isosurfaces of the Q-criterion with a value of 2×10^8 are shown in Fig. 5(b) and are colored by the instantaneous static pressure ratio.

Close-up views of the base region are given in Fig. 5(c) and Fig. 5(d) showing the mean Mach number and the static pressure ratio respectively. At the base shoulder the supersonic flow separates resulting in a subsonic recirculation zone between the base and the strongly expanding plume. The shear layer originating at the base shoulder encloses the recirculation zone on the outer side. Due to the interaction of the plume and the freestream an inner and an outer shock is generated. The mixing of the nozzle flow and the ambient flow takes place in the area labeled as mixing region in between both shocks. The shear layer originating at the base shoulder as well as the nozzle shear layer which is not indicated in the figure pass through the mixing region. The strong expansion of the cold plume is due to the high pressure ratio between the nozzle flow and the freestream.

As can be seen in Fig. 5(b), small vortical structures are present after the separation and are stretched as they leave the low pressure recirculation zone into the higher pressure mixing region between the plume barrel shock (inner shock) and the outer recompression shock.

Schlieren images obtained by the experiments are snapshots of the instantaneous flowfield. To enable a comparison with the mean flow field of the numerical simulation an averaged Schlieren picture made by

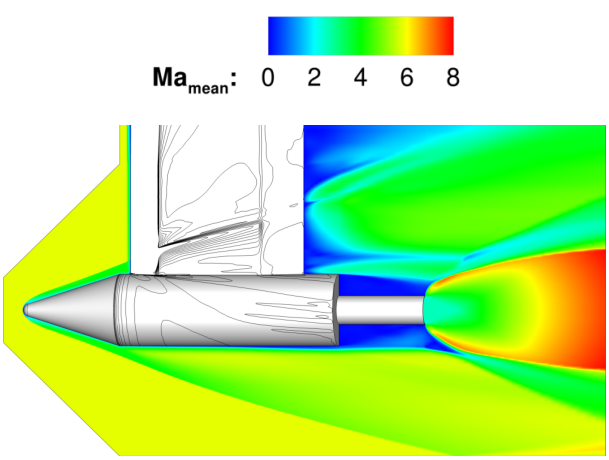

(a) Mean flowfield with pressure ratio contour lines on the main body and the support

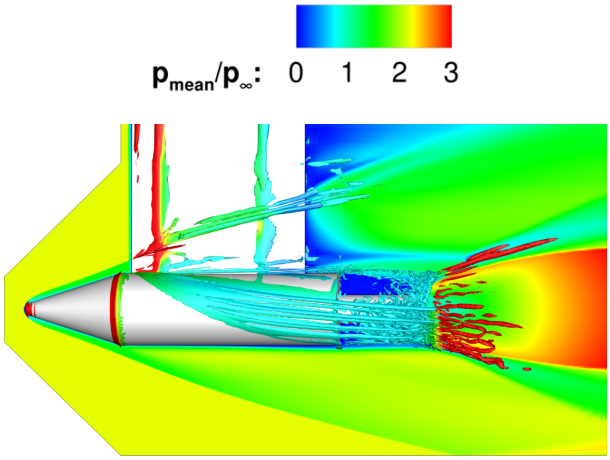

(b) Vortical structures of instantaneous flowfield visualized by isosurfaces of Q-criterion colored by pressure ratio

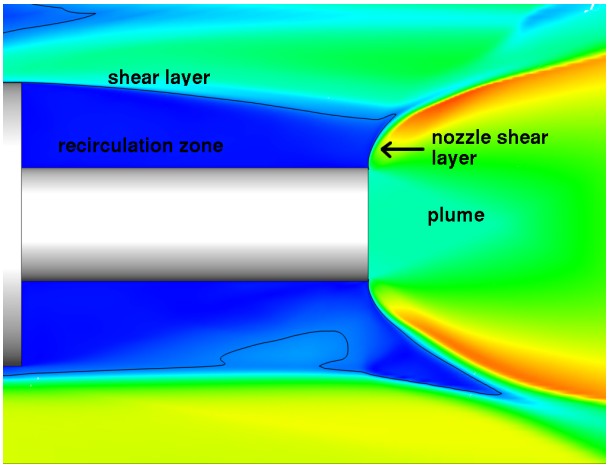

(c) Close-up view of the base region colored by mean Mach number. The black solid line indicates the Mach = 1 line.

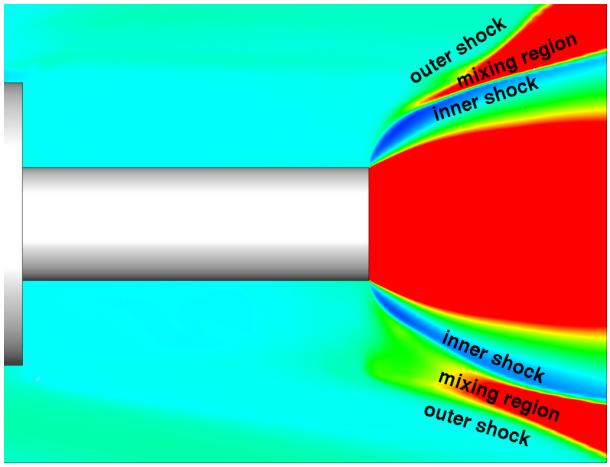

(d) Close-up view of the base region colored by static pressure ratio.

Figure 5: Computed flowfield around the generic rocket model.

image processing out of 30 images from the HLB experiments is shown in Fig. 6. It can be compared with a contour plot of the numerical mean values of the density gradient magnitude in the symmetry plane. The characteristic features of the base flow discussed above like the inner shock of the plume, the outer recompression shock and the mixing region in between those as well as the strong expansion fan of the jet at the nozzle exit can be identified clearly. Deviations between experiment and numerical simulation remain since a Schlieren picture is a line of sight method whereas the contour plot shows only a cut through the three-dimensional flow field. Moreover, the numerical result is extracted from mean values whereas Schlieren pictures are snapshots of the instantaneous flowfield.

4.2 Influence of the support on the base flow

As can be seen by the visualization of the stretched vortices along the main body in Fig. 5(b), the base flow is non-symmetric in circumferential direction due to the interaction of the support and the freestream.

In Fig. 7 contour plots of the time averaged velocity in streamwise direction normalized by the freestream velocity are shown for different positions in axial direction in the base region. The circular shape of the recirculation zone breaks down as the flow moves downstream. This effect is caused by the strong influence of the support. Big vortical structures emanating in the wake of the support shock drive the change of the recirculation zone on the bottom side whereas the freestream flowfield disturbed by the support affects the upper part. So even on the opposite side of the support the flow is heavily influenced by this obstacle. In the center of Fig. 7(e) the circular shape of the plume just downstream of the nozzle exit is visible.

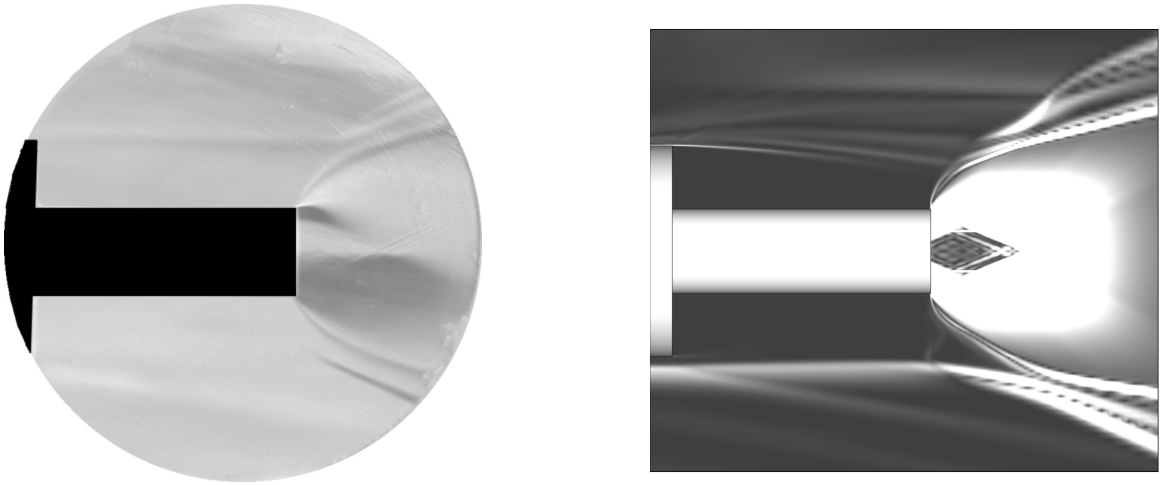

(a) Experiment HLB

(b) Mean value of the IDDES

Figure 6: Averaged Schlieren image of the base flow with plume versus magnitude of the density gradient in the symmetry plane.

4.3 Pitot pressure profiles

The Pitot pressure profiles at the nozzle exit and two nozzle diameters downstream of the exit plane are given in Fig. 8 for the IDDES using time averaged values and experimental data measured in the HLB wind tunnel. The profiles are taken in the vertical plane. Although the experiments achieve the nominal conditions of the ambient flow, the nominal total pressure in the nozzle reservoir is not reached. Therefore, the Pitot pressure profiles are normalized by the total pressure of the nozzle reservoir to enable a good comparison in the plume region. Outside the plume region in Fig 8(b) below $z/D < -1.0$ the normalization causes an artificial difference between the numerical and experimental results. Therefore, the numerical values are repeated there with the same scaling as the experimental values.

The numerical simulation and experiment agree well in the whole vertical plane. Especially, the nozzle flow and the plume expansion are captured in the computation. The asymmetry of the IDDES profile outside the plume region results from the influence of the support as discussed in Sec. 4.2.

4.4 Grid refinement analysis

The grid sensitivity of the nozzle shear layer is analyzed in the numerical simulation. A region enclosing the nozzle shear layer near the nozzle exit is significantly refined leading to a doubling of the overall grid points, Fig. 4(c). The flow topology stays the same as on the original grid. A qualitative view of the unsteady behavior of the refined plume shear layer indicates no fundamental impact of the refinement but a similar stability. A quantitative view is given in Fig. 9 where the pressure signals normalized by the freestream pressure are shown at two locations on the nozzle wall reflecting the unsteadiness of the base flow. These sensors are located on the nozzle dummy on the opposite side of the support (180°), where the first sensor is $56\,mm$ downstream of the base plane and the second sensor has a distance of $83\,mm$ from the base. Normalization of the pressure signal is done by the freestream pressure. The physical time is normalized by a reference time which is defined by $t_{ref} = D/U_\infty$, the main body diameter divided by the streamwise freestream velocity.

The difference between the two signals computed on the original and the adapted grid in both charts arises from the restart of the simulation on the refined grid. For both grids the pressure fluctuations near the nozzle shear layer are in the same order of magnitude. This indicates that the grid resolution of the original grid might be sufficient to generate reasonable solutions for the base flow simulation. However, the solution must be further advanced in time to allow a proper spectral analysis.

4.5 Spectral analysis

In the HLB experiments, the pressure signal is recorded at a sampling rate of 3 MHz and filtered by a Butterworth low-pass filter with a cutoff frequency of 50 kHz. Experimental data is available from twelve

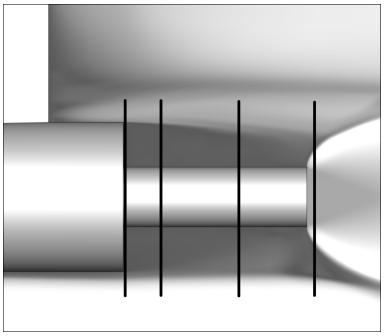

(a) Position of slices (b) to (e) indicated by lines in the base region.

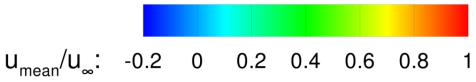

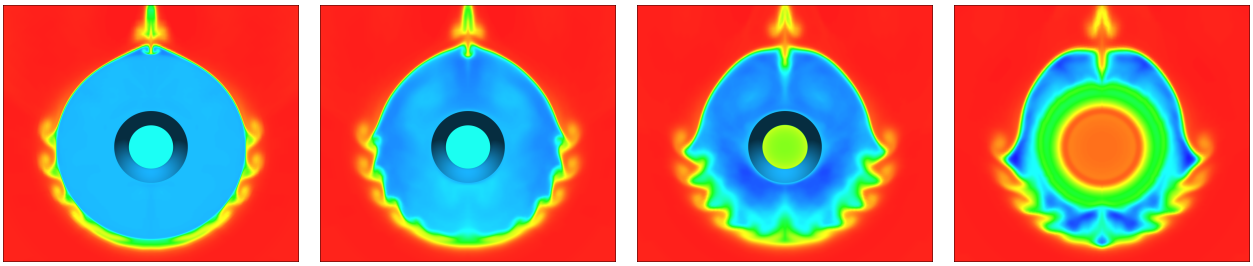

(b) $x/D = 0.01$ (c) $x/D = 0.25$ (d) $x/D = 0.75$ (e) $x/D = 1.25$

Figure 7: Time averaged streamwise velocity normalized by freestream velocity for different positions in the base region. The main body base is located at $x/D = 0$ and the nozzle exit is at $x/D = 1.2$.

shots, each having a length of 40 ms and containing 120000 samples. The pressure signal recorded from numerical data has a total of 65800 samples, which corresponds to 3.29 ms in physical time or roughly 28 t_{ref}, where once again $t_{ref} = D/U_\infty$.

The spectral analysis of the pressure fluctuations p' for several sensor positions on the base is performed by estimating the power spectral density (PSD) using Welch's method. At least ten experimental time traces with 120000 samples each are concatenated for the PSD computation. A Hamming window is applied to each block and the segments have an overlap of 50%. This leads to a resolution of $\Delta f = 25$ Hz in the frequency domain. The PSD of the numerical data is computed using all 65800 samples as one single block and applying a Hamming window as well. Here, the obtained resolution in the frequency domain is $\Delta f = 303$ Hz.

The power spectral density is plotted against the Strouhal number Sr_D, which is defined by the frequency f multiplied by t_{ref}:

$$Sr_D = f \cdot t_{ref} = \frac{fD}{U_\infty}, \tag{3}$$

in which a frequency of 10 kHz corresponds to $Sr_D \approx 1.19$ in the present case.

Only one sensor position matches exactly between the numerical simulation and the experiment, located at $r = 45\,mm$ and $\Phi = 180°$ on the base of the main body but the surrounding values in the experiment and the IDDES show a similar behaviour. In Fig. 10(a), numerical and experimental pressure spectra are plotted for this location.

Near the origin, the experimental spectrum has a high peak much greater than the maximum ordinate in the plot. The amplitude of the spectrum drops fast until a small plateau can be identified in the range of $Sr_D = 0.1 \div 0.3$. The amplitude decays further without any distinct peaks up to a Strouhal number of about 0.75. For higher Strouhal numbers, the amplitude level rises about one order of magnitude, showing several peaks in the range up to $Sr_D = 2$. These peaks can be addressed to the influence of the plume on the base flow since spectra from experiments without plume do not show any peaks in this range [13]. At $Sr_D = 1.8$, a distinct peak is visible after which the same amplitude level is reached as before.

The spectrum generated from numerical results is much coarser. Between Strouhal numbers 0.15 and 0.3, the curve coincides quite well with the amplitude level of the experimental spectrum. Like in the experiment, the amplitude level drops but shows no rise at $Sr_D = 0.75$. In contrast, the amplitude stays at the same level which is roughly two orders of magnitude below the experimental level for higher Strouhal numbers. In addition, no distinct peaks can be identified in the spectrum for the IDDES results in this range contrary to

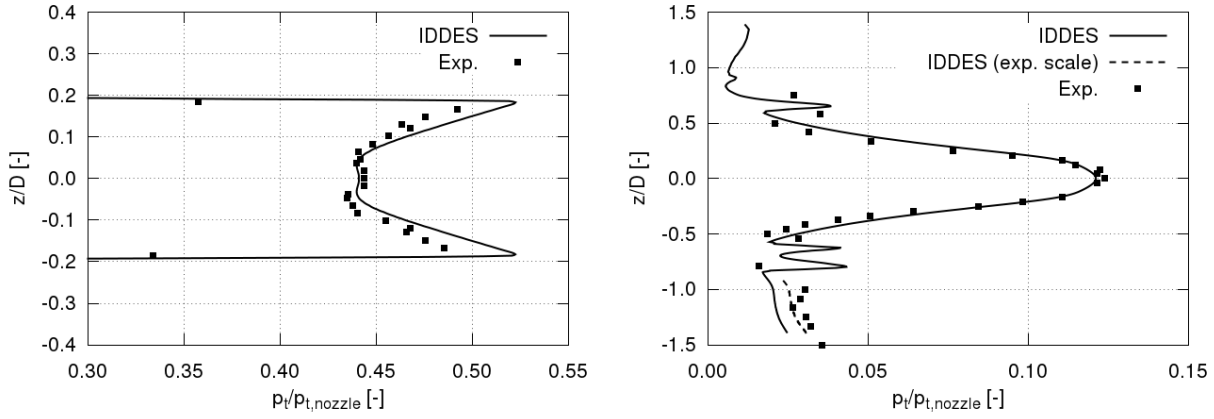

(a) $x/D = 1.2$ (b) $x/D = 2$

Figure 8: Pitot pressure profiles of the plume in vertical direction: HLB measurements and IDDES results. The normalization factors are $p_{t,nozzle} = 16.13\,bar$ for the experimental data and $p_{t,nozzle} = 20\,bar$ for the numerical result.

the curve of experimental data.

Pressure spectra from numerical data are shown in Fig. 10(b) for different azimuthal positions at a radius of $40\,mm$ on the base of the main body. The first sensor lies in the symmetry plane on the opposite site of the support, denoted by 180° in the figure. Results for two other sensors at 190° and 240° as depicted in Fig. 3(b) are plotted as well.

The sensor in the symmetry plane at 180° and the sensor at 190° show an almost identical behavior. For the outer sensor located at 240° on a radius of $40\,mm$ the peaks up to a Strouhal number of 0.3 are slightly lower but at the same abscissas. No drop in the amplitude at about $Sr_D = 0.35$ is found for the latter sensor. Overall, the amplitude level of this spectrum is almost one order of magnitude lower for higher Strouhal numbers than the spectra for sensors near the symmetry plane.

Spectra of experimental data are presented in Fig. 10(c) for sensors with the same azimuthal position as in Fig. 10(b), but for a different radius on the base. The level of amplitude in the spectra of sensor position 190° and 240° follows a similar trend over the whole Strouhal number domain as for the sensor on the symmetry plane. No drop in amplitude occurs at $Sr_D = 1.2$ for the sensor at 240° which is the most recognizable difference between all three curves, next to a slightly higher drop in amplitude level of the curves outside the symmetry plane up to a Strouhal number of 0.75.

One major difference between the numerical and the experimental signals is their length of recorded physical time where the computed signal has only less than 10% of the experimental one. Since the number of nodes in the spectra is directly linked to the length of the input signal, the resolution of the IDDES result in the low frequency range is very coarse. A longer calculation would improve the representation of the IDDES in this regime, but the major peaks at low frequencies observed in the IDDES but not in the HLB results will be persistent in successive evaluations. Although the geometry and farfield is symmetric with respect to the plane including the support, the unsteady physical flowfield is not bound to share this symmetry. Therefore, a continuation of the simulation including the symmetry plane promises only a limited benefit.

Another difference is the level of the amplitude of the recorded pressure fluctuations. The maximum amplitude in the simulation for this location is at about $40\,Pa$, and the rms value of the computational signal is approximately $12.5\,Pa$. In contrast, the experimental signal exhibits five times larger amplitudes and the rms value is around $130\,Pa$.

5 Concluding remarks

A generic rocket launcher configuration is investigated experimentally and numerically. The Pitot pressure profiles measured through the plume in the HLB show good agreement with mean values extracted from the IDDES calculations with the DLR-TAU code. A spectral analysis of unsteady surface pressure signals on the base reveals deviations between the experiment and the numerical simulation which are not fully understood

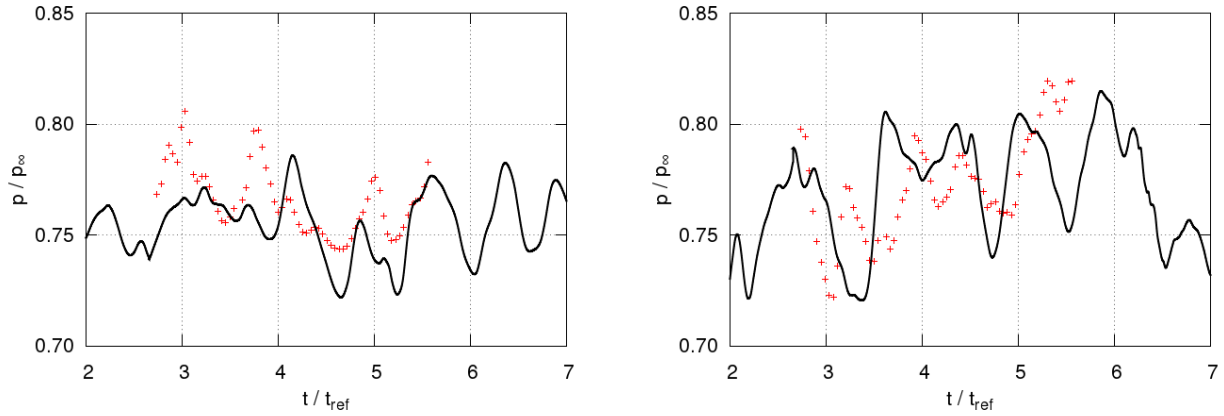

(a) $x = 56\,mm, \phi = 180°$ (b) $x = 83\,mm, \phi = 180°$

Figure 9: Comparison of computed normalized pressure signals over time for the simulation on the original and on the refined grid. Results computed on the original grid are represented by the solid lines and results of the refined grid are depicted by crosses.

so far. Although the results are not conclusive at the current stage of the investigation they provide useful indications for further steps.

Acknowledgments

The numerical group thanks our former DLR colleague Yancheng You for providing the original grid and starting solution for the shown IDDES.

The collaboration of the numerical and experimental working groups is established within the framework of the Sonderforschungsbereich Transregio 40 *"Technological foundations for the design of thermally and mechanically highly loaded components of future space transportation systems"* and is financially supported by the German Research Foundation.

References

[1] Hannemann, K., Lüdeke, H., Pallegoix, J.-F., Ollivier, A., Lambare, H., Maseland, J.E.J., Geurts, E.G.M., Frey, M., Deck, S., Schrijer, F.F.J., Scarano, F. and Schwane, R. 2011. Launch Vehicle Base Buffeting Recent Experimental and Numerical Investigations. *Proceedings 7th European Symposium on Aerothermodynamics for Space Vehicles, 9-12 May 2011, Brugge, Belgium.*

[2] You, Y., Buanga, B., Hannemann, V. and Lüdeke, H. 2011. Evaluation of Turbulence Models in Predicting Hypersonic and Subsonic Base Flows using Grid Adaptation Technique. *Chinese Journal of Aeronautics.*

[3] Saile, D., Gülhan, A., Henckels, A., Glatzer, C., Statnikov, V., Meinke, M. 2011. Investigations on the Turbulent Wake of a Generic Space Launcher Geometry in the Hypersonic Flow Regime. *Proceedings of the 4th European Conference for Aerospace Sciences (EUCASS), Saint Petersburg, Russia, July 4-8 2011.*

[4] Wolf, C.C., You, Y., Hörnschemeyer, R., Lüdeke, H. and Hannemann, V. 2011. Base-flow sensitivity of a generic rocket forebody towards small freestream angles. *Proceedings of the 4th European Conference for Aerospace Sciences (EUCASS), Saint Petersburg, Russia, July 4-8 2011.*

[5] Casper, M., Stephan, S., Windte, J., Scholz, P., Radespiel, R., Scharnowski, S., Kähler, C.J. 2012. *Proceedings of the 28th Aerodynamic Measurement Technology, Ground Testing, and Flight Testing Conference, New Orleans, Louisiana, USA, June 25-28 2012.*

[6] Mack, A. and Hannemann, V. 2002. Validation of the unstructured DLR-TAU Code for Hypersonic Flows. *AIAA 2002-3111.*

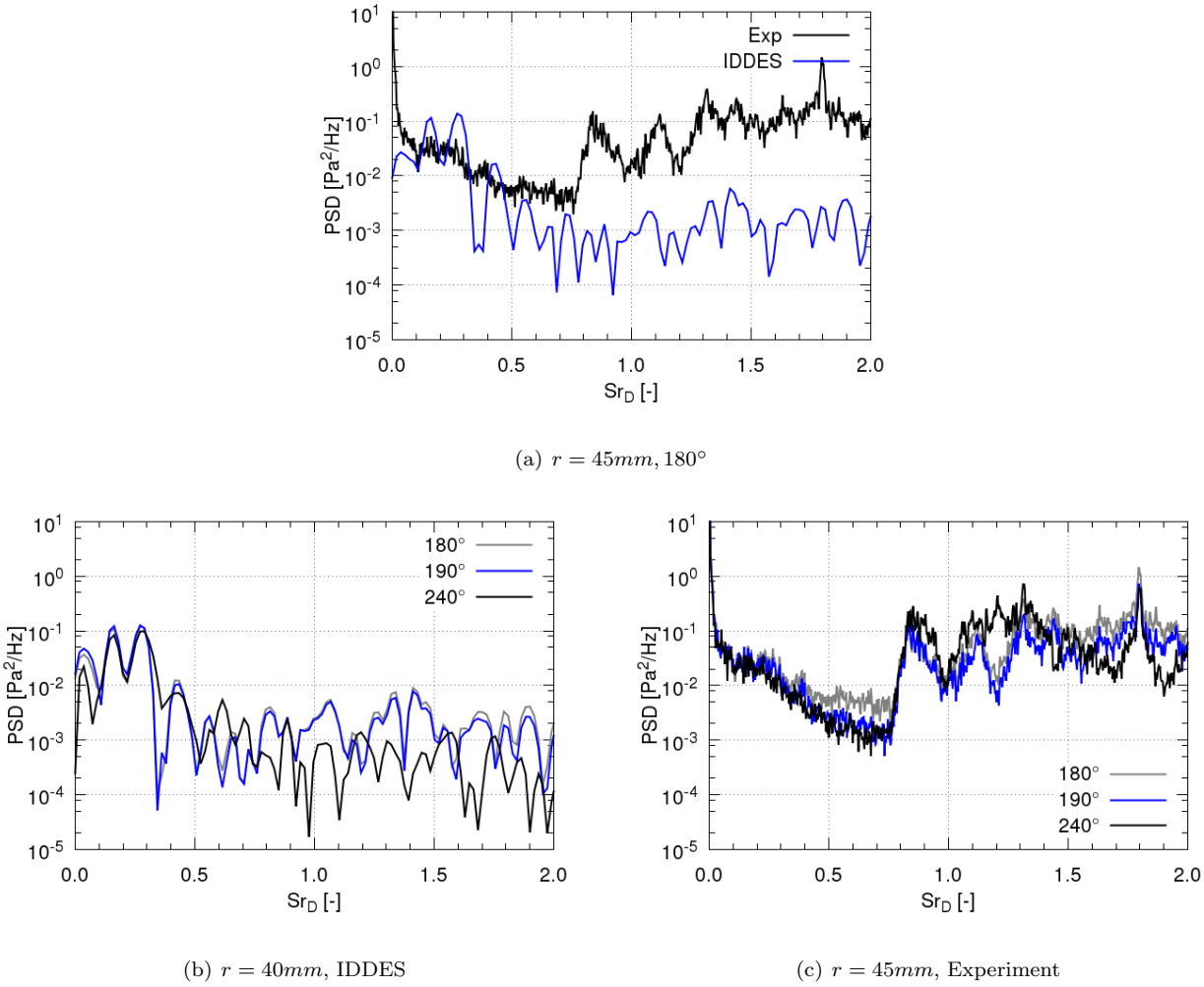

(a) $r = 45mm, 180°$

(b) $r = 40mm$, IDDES

(c) $r = 45mm$, Experiment

Figure 10: Spectral analysis of the pressure fluctuations.

[7] Reimann, B., Johnston, I. and Hannemann, V. 2004. DLR-TAU Code for High Enthalpy Flows *Notes on Numerical Fluid Mechanics and Multidisciplinary Design.* 87:99-106, Springer DE.

[8] Thornber, B., Mosedale, A., Drikakis, D., Youngs, D. and Williams, R.J.R. 2008. An improved reconstruction method for compressible flows with low Mach number features. *Journal of Computational Physics* 227:4873-4894.

[9] Bauer, M. , Birken, P., Hannemann, V. and Oßwald, K. 2013. Accuracy in a finite volume Godunov type method. In: A. Dillmann, G. Heller, H.-P. Kreplin, W. Nitsche, I. Peltzer (eds.). *New Results in Numerical and Experimental Fluid Mechanics VIII.* 387-394.

[10] Travin,A., Shur, M., Spalart, P. and Strelets, M. 2006. Improvement of delayed detached-eddy simulation for LES with wall modelling. In: P. Wesseling, E. Oate, J. Priaux (eds.). *Proceedings of the European Conference on Computational Fluid Dynamics ECCOMAS CFD 2006, Egmond aan Zee, The Netherlands.*

[11] Mockett, C. 2009. A comprehensive study of detached-eddy simulation. PhD Thesis. Technische Universität Berlin.

[12] Estorf, M., Wolf, T. and Radespiel, R. 2005. Experimental and Numerical Investigations on the Operation of the Hypersonic Ludwieg Tube Braunschweig. In: *Proceedings of the 5th European Symposium on Aerothermodynamics for Space Vehicles, ESA SP-563.* 579–586.

[13] Stephan, S., Radespiel, R. and Müller-Eigner, R. 2012. Jet Simulation Facility using the Ludwieg Tube Principle. *Proceedings of the 5th European Conference for Aerospace Sciences (EUCASS), Munich, Germany, July 1-5 2013.*